IEEE Access
Multidisciplinary | Rapid Review | Open Access Journal

Received 7 May 2024, accepted 1 July 2024, date of publication 10 July 2024, date of current version 23 July 2024.

Digital Object Identifier 10.1109/ACCESS.2024.3426330

APPLIED RESEARCH

Development and Control of PMSM Drive With Improved Performance Over Wide Speed and Load Ranges

YI-SHI LIN[1], CHEN-WEI YANG[1], CHANG-MING LIAW[1], (Member, IEEE), CHANG-LIN CHIANG[2], YANG-GUANG LIU[2], AND CHIEN-CHANG WANG[2]

[1]Department of Electrical Engineering, National Tsing Hua University, Hsinchu 300044, Taiwan
[2]Industrial Technology Research Institute, Hsinchu 300044, Taiwan

Corresponding author: Chang-Ming Liaw (cmliaw@ee.nthu.edu.tw)

This work was supported by the Bureau of Energy and Energy Administration, Ministry of Economic Affairs, Taiwan.

ABSTRACT Generally, an inverter fed motor drive is often operated under low speed and/or light loads. Hence, except for good driving characteristics, having evenly high efficiencies over wide load range is also critical for a high-performance motor drive. A dual-inverter fed permanent-magnet synchronous motor (PMSM) drive achieving these goals is developed in this paper. First, the single-inverter fed drive is established with properly designed intelligent power module (IPM) based inverter schematic and control schemes. The dynamic modeling and systematic controller designs for current and speed control schemes are presented. Satisfactory dynamic and steady-state operating performances are verified experimentally. Next, the dual-inverter fed PMSM drive is constructed. The current sharing control and zero-sequence harmonic suppression approaches are proposed to yield improved performance. The robust current control is proposed to enhance the harmonic suppression response. Through the developed current robust error cancellation controller (CRECC), the robust and faster cancellation response is yielded. Finally, the motor drive efficiencies affected by power level, IPM type, inverter cell number, switching frequency, and DC-link voltage level are comparatively evaluated by measured results. Accordingly, the evenly high composite efficiencies over wide speed and load ranges are arranged.

INDEX TERMS PMSM, efficiency, light load, varied voltage, dual inverter, current sharing, zero-sequence, harmonic suppression, robust control.

I. INTRODUCTION

Motor drives are extensively used in various industrial facilities. An inverter fed motor drive with satisfactory performance can only be achieved via the properly designed power circuit and control schemes. In addition, energy saving and increased efficiency are also the key indices. Generally, motor drive is often operated under low speed and light load conditions. For a pump system, the load will become very light with the reduced speed automatically, since its load power is proportional to the cubic of speed. Hence, high efficiency over wide speed range is an important issue and received much attention recently. However, energy conversion efficiencies of motor drive are highly affected by many factors. The IPM based inverter with larger rating will have lower efficiency under lighter loads. Therefore, adopting dual paralleled IPM inverters with lower rating can yield high efficiencies over wide load range through working module number selection. Moreover, the fault-tolerant ability is possessed. Although the initial cost of dual-inverter with two smaller rated IPMs is slightly higher, then the single-inverter using larger rated IPM, the saved electricity fee due to higher efficiency will be compensated gradually. However, many issues should be properly treated for paralleled PWM inverters.

With the advancement of technology, paralleled three-phase inverters have begun to find applications in various high-power scenarios [1], [2], [3], [4], [5]. In [1], the multiple high-frequency resonant inverters are connected in parallel

The associate editor coordinating the review of this manuscript and approving it for publication was Mou Chen.

to the high-frequency high-voltage low-current AC-bus. The circul- ation current minimization is achieved by regulating the active and reactive currents. As to [2], the multiple inverters are controlled to feed the required powers to the utility grid. The circulation current is suppressed using a linear quadratic integral regulator. Paralleling the inverters can lead to issues arising from mismatches between them, resulting in circulating currents [6], [7], [8]. These circulating currents not only lead to unnecessary energy consumption but also make the system more prone to instability. Typically, these circulating currents can be divided into high-frequency components, closely related to the switching frequency, and low-frequency components, which align with the fundamental frequency. High-frequency circulating currents can be mitigated using inductors, while low-frequency circulating currents are effectively managed through active control methods, allowing for a reduction in the size of passive components.

Circulating current is generated due to the paralleled unbalanced loads, leading to uneven zero-sequence modu- lation signals in the inverter. While PI controllers have been utilized to these modulation signals and eliminate circulating currents [3], [9], [10], they have limited bandwidth, resulting in delayed responses. In [10], a circulating current control method designed for directly paralleled inverters is proposed. Since the treated variables belong to DC variables in the transformed domain, this method effectively eliminates the bandwidth limitations of the PI controller in the 0-axis current loop. The feedforward zero-sequence modulation signals are not needed.

For establishing a high-performance PMSM drive, some key typical affairs must be properly treated, including parameter estimation [11], inverter power circuit establish- ment, rotor position sensing, commutation setting, current control [12], and speed control [13]. In [13], an improved robust finite control set predictive current control algorithm for PMSM drives is presented. The performance degradation due to parameter mismatch is improved by a sliding mode stator current and disturbance observer. Furthermore in [14], the key problems in the finite control set model predictive control scheme are explored. The performance improvement schemes are reviewed, and the possible research trend is suggested.

This paper presents a dual-inverter powered PMSM drive with good driving performance and evenly high efficiencies in wide speed/load ranges by considering many key issues. The IPM-based high-performance single-inverter fed motor is first established. Except the power circuit, sensing and PWM switching schemes, the dynamic current and speed control schemes are properly designed. The dynamic modeling and systematic controller design are detailedly presented. Then the dual-inverter fed motor drive is constructed. Good current sharing and zero-sequence current suppression characteristics are achieved by the proposed control technologies. For the latter affair, the cause and dynamic modeling for zero-sequence circulating current are first made. Then, the extracted 3rd-order harmonics from the sensed zero-sequence current are processed and transformed to the harmonic rotating d-q frame resulting in DC quantities. The bandwidth limitation possessed by the PI-controller can be avoided. In addition, the proposed CRECC is applied to yield the enhanced current suppression response and robustness. The theoretical basis and robustness analysis of the CRECC are presented. Under satisfactory driving characteristics, the key factors affecting the efficiency of the dual-inverter fed PMSM drive are explored experimentally in detail. The factors include IPM types, number of acting inverters, DC-link voltage, and switching frequency, etc. Accordingly, the evenly high energies of the motor drive over wide speed/load ranges are presented by the proper arrangement and verified experimentally.

List of major contributions

Single-inverter fed PMSM drive
(1) Establishment of IPM-based inverter fed PMSM drive. (2) Current and speed dynamic controls: ● Dynamic modeling. ● Quantitative controller design. ● Motion driving performance evaluation. (3) Steady-state characteristics exploration: Key effects on motor drive efficiencies are explored: IPM ratings, DC-link voltage level, back-EMF effects, load levels, and switching frequency.
Double-inverter fed PMSM drive
(1) IPM-based power circuit establishment. (2) Good current sharing control. (3) Zero-sequence circulating current suppression control: ● Equivalent circuit derivation with circulation current behavior. ● 3rd-order harmonic current extraction and two-phase currents generation. ● 3rd-order harmonic rotating frame transformation to yield equivalent DC-quantity for avoiding the bandwidth limitation possessed by PI controller. ● The CRECC is proposed to increase the harmonic suppression performance by PI control: Theoretical analysis, robustness proof, and effectiveness experiment verification. (4) Steady-state efficiency enhancement exploration: ● The studied key affecting factors: speed range, power level, IPM type, inverter working number, switching frequency, DC-link voltage level. ● Dual-inverter fed PMSM drive operation arrangement for achieving evenly highly efficiencies over wide speed and load ranges.

II. SINGLE-INVERTER FED IPMSM DRIVE

A. POWER CIRCUIT

Figs. 1(a) and 1(b) show the power circuit and control scheme of the established DSP-based single inverter fed IPMSM drive. A three-phase permanent-magnet synchronous generator (PMSG) followed by a three- phase diode rectified resistor is served the dynamic load.

The specifications and measured parameters of the used IPMSM obtained from the data sheet and the experimental estimation are listed in Table 1. And the employed SPMSG is rated as three-phase, 4-pole, Y- connected, 1.7kW, 4500rpm.

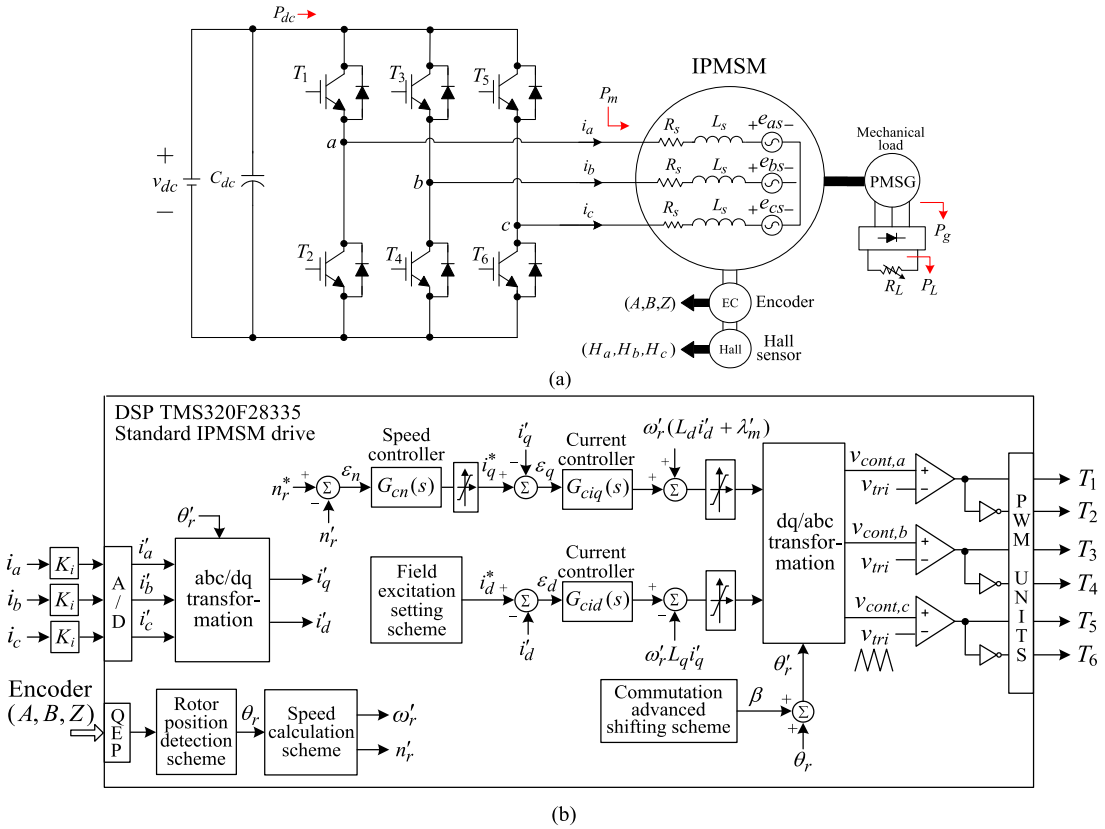

FIGURE 1. The established single-inverter fed IPMSM drive: (a) power circuit; (b) control scheme.

The six-pack IGBT IPM is employed to construct the motor drive inverter for compactness. Normally, IGBT IPM inherently possess low efficiency under extremely light load. To comparatively explore this feature experimentally, the following two typical off-the-shelf IPMs with different current ratings (Mitsubishi, Japan) are adopted:

- PSS10S92: $I_c = 10$A(DC), 20A(Peak), 600V.
- PSS20S92: $I_c = 20$A(DC), 40A(Peak), 600V.

B. CONTROL SCHEME

1) CURRENT-CONTROLLED PWM SCHEME

The current loop control blocks of the developed IPMSM drive in d-q domain are shown in Fig. 2. The ramp-comparison current-controlled PWM (RC-CCPWM) scheme is adopted. The PWM control commands (v_q^*, v_d^*) consist of the feedback regulated components (v_{qb}^*, v_{db}^*) and the feed-forward back-EMF elimination components (v_{qf}^*, v_{df}^*), where $v_{qf}^* = \omega_r'(L_d i_d' + \lambda_m')$ and $v_{df}^* = \omega_r' L_q i_q'$ as indicated in Fig. 2. The motor parameters can be found in Table 1, and the others are set as: switching frequency $f_s = 20$kHz, $K_i = 0.04$V/A, $K_{pwm} = V_{dc}/2$.

The current feedback controllers are chosen to be PI type:

$$G_{ciq}(s) = K_{Pi_q} + \frac{K_{Ii_q}}{s} \tag{1}$$

$$G_{cid}(s) = K_{Pi_d} + \frac{K_{Ii_d}}{s} \tag{2}$$

TABLE 1. Key parameters of the employed IPMSM.

Quantity	Conversion from Gaussian and CGS EMU to SI [a]
YELI Electric	IPMSM
Models	IP-S71-135 (6P)
Rated power	1kW
Rated torque	3.23Nm
Rated speed	3000rpm
Rated current	4.8A_{rms}
Phase winding resistance	$R_s = 0.85\Omega$
Phase winding inductance	$L_s = 5.255$mH ($L_q = 6.695$mH, $L_d = 3.815$mH)
Peak of flux linkage	$\lambda_m' = 0.12938$Wb
Phase back-EMF constant	$k_e = 28.74\text{V}_{\text{rms}}$/krpm

The pole-zero cancellation method is applied to design the current controllers. From Fig. 2 the current loop-gains of the d-axis and q-axis can be derived and set to be:

$$T_{iq}(s) = G_{ciq}(s)K_{pwm}\frac{1}{sL_q + R_s}K_i = \frac{2\pi f_c}{s} = \frac{\omega_c}{s} \tag{3}$$

$$T_{id}(s) = G_{cid}(s)K_{pwm}\frac{1}{sL_d + R_s}K_i = \frac{2\pi f_c}{s} = \frac{\omega_c}{s} \tag{4}$$

These will yield the current closed-loop tracking transfer function of $T_{ic}(s) = \omega_c/(s + \omega_c)$ without steady-state error.

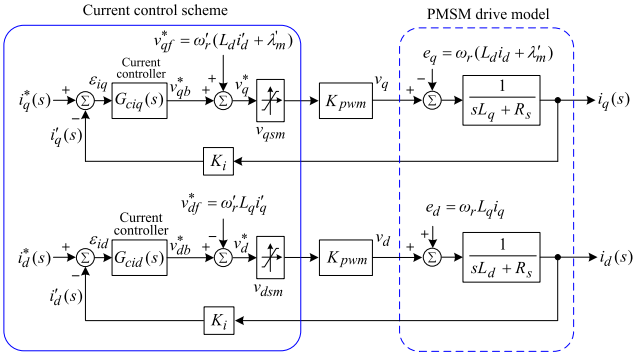

FIGURE 2. Current loop control blocks of IPMSM drive in dq-frame.

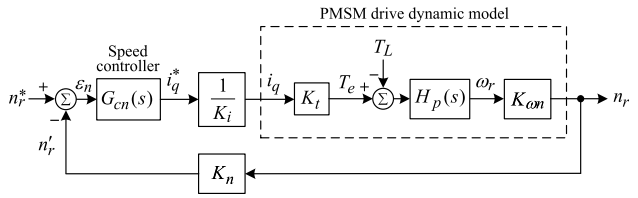

FIGURE 3. Speed loop control block.

By letting the crossover frequency be $f_c = 1$kHz, one can find:

$$K_{Iiq} = K_{Iid} = \frac{2\pi f_c R_s}{K_i K_{pwm}} = 890.118 \tag{5}$$

$$K_{Piq} = \frac{K_{Iiq} L_q}{R_s} = 12.247, K_{Pid} = \frac{K_{Iid} L_d}{R_s} = 9.231 \tag{6}$$

2) SPEED CONTROL SCHEME

Having designed the current control loop, the dynamic modeling and quantitative controller design for the speed loop are conducted.

a: DYNAMIC MODEL ESTIMATION

The speed loop control block of the IPMSM drive is shown in Fig. 3. The related system parameters are set as: speed sensing factor ($K_n = 2.5 \times 10^{-4}$V · min/rev), current sensing factor ($K_i = 0.04$V/A),$K_{\omega n}$ = rad/s to rpm transfer ratio ($K_{\omega n} = 60/2\pi = 9.55$rpm · s/rad). The torque generating constant can be obtained as:

$$K_t = \frac{3}{2}\frac{P}{2}\lambda_m^{'r} = 0.5822\text{N} \cdot \text{m/A} \tag{7}$$

And the plant dynamic model is:

$$H_p(s) = \frac{1}{Js + B} \triangleq \frac{b}{s + a}, \quad a \triangleq \frac{B}{J}, \quad b \triangleq \frac{1}{J} \tag{8}$$

The step response method is employed to estimate the dynamic model parameters. The speed feedback controller is chosen to be the proportional type $G_{cn} = K_{Pn}$. The speed response can be derived from Fig. 3 as:

$$n_r = G_{dr}(s)\Delta n_r^* + G_{dd}(s)\Delta T_L \tag{9}$$

where

$$G_{dr}(s) \triangleq \frac{\Delta n_r(s)}{\Delta n_r^*(s)}\bigg|_{\Delta T_L(s)=0} = \frac{bK_{Pn}K_tK_{\omega n}/K_i}{s + a + bK_{Pn}K_tK_nK_{\omega n}/K_i} \triangleq \frac{h}{s+u} \tag{10}$$

$$G_{dd}(s) \triangleq \frac{\Delta n_r(s)}{\Delta T_L(s)}\bigg|_{\Delta n_r^*(s)=0} = \frac{-bK_{\omega n}}{s + a + bK_{Pn}K_tK_nK_{\omega n}/K_i} \triangleq \frac{-bK_{\omega n}}{s+u} \tag{11}$$

$$h = bK_{Pn}K_tK_{\omega n}/K_i,\ u = a + hK_n \tag{12}$$

Let $K_{Pn} = 0.5$ and the load resistance in Fig. 1 be $R_L = 50\Omega$, and the IPMSM be initially operated at $n_r = 2700$rpm, the measured speed response due to a step speed command change $\Delta n_r^* = 300$rpm is depicted in Fig. 4. From the result, it can find that the steady-state speed is 2962.5rpm ($\Delta n_r = 262.5$rpm) and the rise time τ_n at $0.632\Delta n_r$ is 130ms. Hence one can derive to obtain the following estimated dynamic model parameters:

$$a = 0.9615, b = 387.4 \tag{13}$$

$$J = 2.5813 \times 10^{-3}\text{kg} \cdot \text{m}^2 \tag{14}$$

$$B = 2.4819 \times 10^{-3}\text{N} \cdot \text{m} \cdot \text{s/rad} \tag{15}$$

Accordingly, the estimated dynamic model transfer function is:

$$K_tH_p(s) \triangleq \frac{\Delta\omega_r}{\Delta i_q} = \frac{K_t b}{s + a} = \frac{225.55}{s + 0.9615} \tag{16}$$

The simulated response at the same condition has been made (not shown here) for verifying its closeness to the measured one.

b: SPEED CONTROLLER DESIGN

In the proposed speed control scheme shown in Fig. 3, the speed controller is chosen to be the PI type:

$$G_{cn}(s) = K_{Pn} + \frac{K_{In}}{s} \tag{17}$$

The closed-loop speed tracking transfer function can be derived as:

$$H_{dr}(s) \triangleq \frac{\Delta n_r(s)}{\Delta n_r^*(s)} = \frac{bK_{Pn}K_tK_{\omega n}/K_i(s + K_{In}/K_{Pn})}{s^2 + (a + bK_{Pn}K_tK_nK_{\omega n}/K_i)\,s + bK_{In}K_tK_nK_{\omega n}/K_i} \tag{18}$$

The desired speed command tracking response is defined by a first-order transfer function:

$$H_{dr}(s) = \frac{K_n r_n}{s + K_n r_n} = \frac{1}{1 + s\tau_{nde}} \tag{19}$$

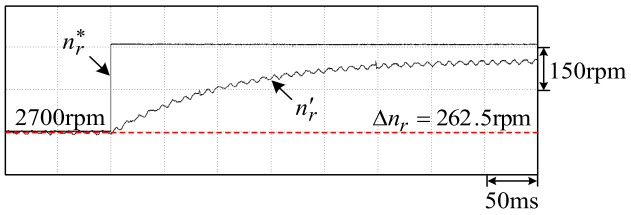

FIGURE 4. Measured speed response by $G_{cn}(s) = K_{Pn} = 0.5$ due to a step speed command change $\Delta n_r^* = 300$rpm at ($v_{dc} = 300$V,$n_r = 2700$rpm, $R_L = 50\Omega$).

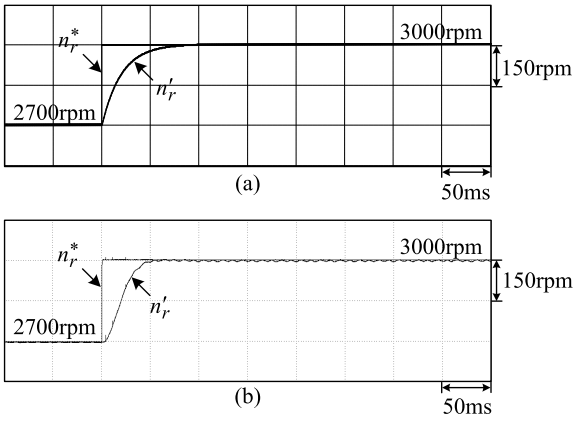

FIGURE 5. Speed responses by the designed PI controller due to a step speed command change of 300 rpm at ($v_{dc} = 300$V,$n_r = 2700$rpm, $R_L = 50\Omega$): (a) simulated result; (b) measured result.

From (18) and (19), the speed PI controller parameters can be derived as:

$$K_{Pn} = \frac{K_i}{K_t K_n b \tau_n}, K_{In} = aK_{Pn} \tag{20}$$

By choosing τ_{nde} =0.02, the speed controller can be found as:

$$G_{cn}(s) = K_{Pn} + \frac{K_{In}}{s} = 3.7143 + \frac{3.5713}{s} \tag{21}$$

The simulated and measured speed tracking responses by the designed controller due to a step command change of 300rpm are shown in Fig. 5(a) and Fig. 5(b). The correctness of the designed controller can be verified from the results.

At the condition (n_r = 3000rpm, v_{dc} = 300V), Fig. 6 shows the measured n_r' and (i_q^*, i_q') of the established IPMSM due to a step load change $R_L = 50\Omega \rightarrow 40\Omega$. Well load speed regulation response can also be confirmed.

3) ACCELERATION/DECELERATION AND REVER-SIBLE OPERATION

The measured (n_r^*, n_r') and (i_q^*, i_q') of the established IPMSM drive accelerating from 0 to 3000rpm and decelerating from 3000rpm to 0rpm under three ramping rates at (v_{dc} = 300V,$R_L = 50\Omega$) are plotted in Fig. 7.

Fig. 8 shows the measured (n_r^*, n_r') and (i_q^*, i_q') at (v_{dc} = 300V,R_L = 50Ω) due to speed command change from n_r^* =3000rpm to -3000rpm with the changing rate of 6000rpm/s. To let the IPMSM drive be reversibly operated, the reversal of torque current can be seen from the results.

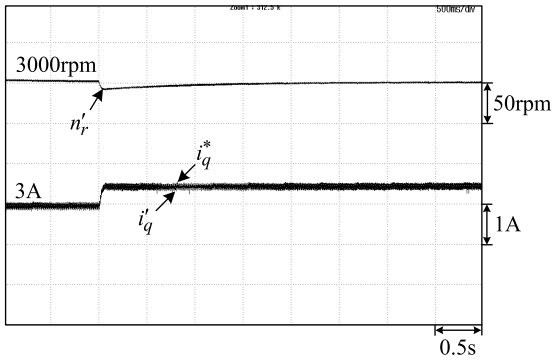

FIGURE 6. Measured (n_r', (i_q^*, i_q')) of the developed IPMSM drive due to a step load resistance change of $R_L = 50\Omega \rightarrow 40\Omega$ at ($n_r^* = 3000$rpm, $v_{dc} = 300$V).

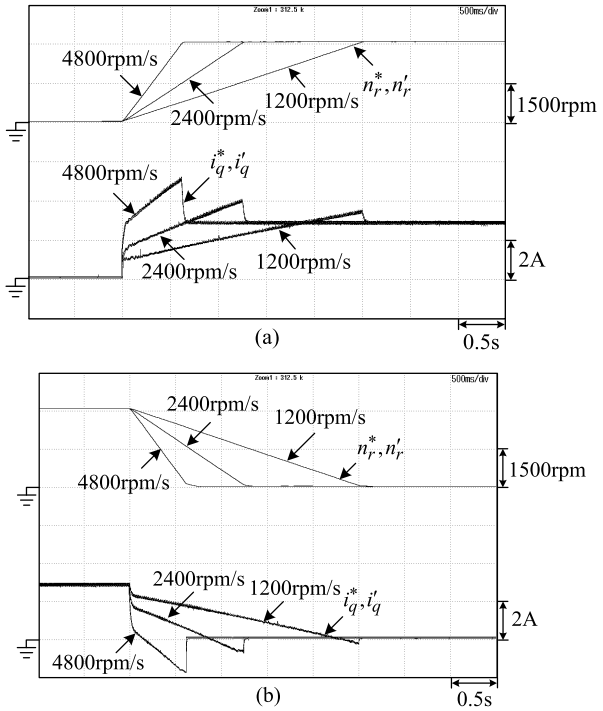

FIGURE 7. Measured (n_r^*, n_r'), (i_q^*, i_q') of the established IPMSM drive during the accelerating and decelerating processes with three speed changing rates at ($v_{dc} = 300$V, $R_L = 50\Omega$): (a)n_r = 0rpm to 3000rpm; (b)n_r = 3000rpm to 0rpm.

From Fig. 7 and Fig. 8, the smooth speed tracking responses during the starting and reversible operations can be seen from the results.

4) STEADY-STATE CHARACTERISTICS

The measured steady-state (i_a, i_b, i_c) of the IPMSM drive at (n_r^* = 3000rpm,v_{dc} = 300V,P_L = 1kW) are shown in Fig. 9. Good sinusoidal current waveforms can be observed from the results.

III. DUAL-INVERTER FED IPMSM DRIVE

A. SYSTEM CONFIGURATION

Fig. 10(a) shows the power circuit of the developed dual-inverter fed IPMSM drive. The inductors L_n = 3mH are added to limit the circuiting current. The proposed control

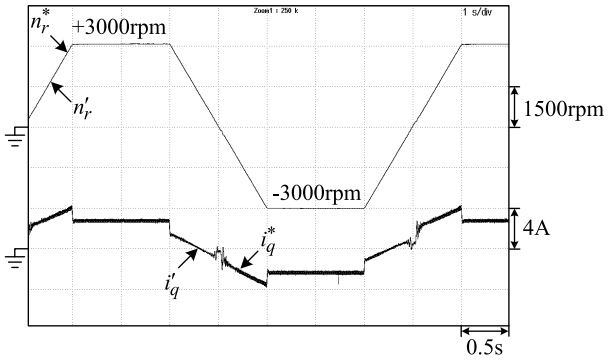

FIGURE 8. Measured (n_r^*, n_r'), (i_q^*, i_q') of the developed IPMSM drive due to speed command change of (n_r = 0rpm→3000rpm→0rpm→ -3000rpm→0rpm) under (v_{dc} = 300V, R_L = 50Ω).

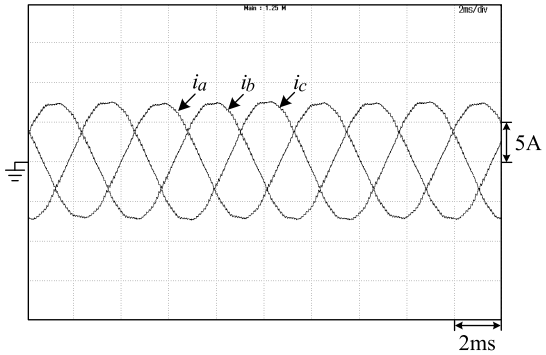

FIGURE 9. Measured steady-state (i_a, i_b, i_c) of the developed IPMSM drive at (n_r^* = 3000rpm, v_{dc} = 300V, P_L = 1kW).

scheme with zero-sequence current suppression scheme is depicted in Fig. 10(b). And the experimental setup photo is shown in Fig. 10(c). The major features are briefly described as follows: (1) The total q-axis torque current comment i_q^* is yielded from the common outer speed loop, then the ones for the primary and secondary inverters are set as $i_{qs}^* = i_{qm}^* = 0.5i_q^*$ for the employed two identical IGBT IPMs. The satisfactory current sharing characteristics are preserved for the properly designed current control schemes of the two single inverters; (2) For the paralleled inverters, the zero-sequence circulating current will inherently exist with the dominant 3rd-order harmonics. The zero-sequence current suppression scheme is proposed to effectively reduce this problem. The control flowchart of the developed dual-inverter fed PMSM drive is shown in Fig. 10(d).

B. ZERO-SEQUENCE CURRENT SUPPRESSION

1) DYNAMIC MODELING

Through careful derivation from Fig. 10(a) one can yield the equivalent circuits in dq domain of dual paralleled inverters as shown in Fig. 11, the variable dx denotes the duty ratio in x-axis generated by the corresponding PWM control signal $v_{cont,x}$. In this arrangement, except for the coupling effects between d-axis and q-axis, there is also a coupling between the two converters. Notably, for the 0-axis, it is encompassed within a closed loop, thereby establishing a path for zero-sequence circulating current. Hence, if there exists a discrepancy between the two paralleled inverters "$d_{01}v_{dc}$" and "$d_{02}v_{dc}$", the circulating current will flow between the inverters.

The zero-sequence current is detected by the sensed primary inverter output currents as:

$$i_{0m} = \frac{1}{3}(i_{am} + i_{bm} + i_{cm}) \tag{22}$$

It is important to note that the circulating current i_{om}' consists of odd harmonic currents. Obviously, the dominant components are 3rd-order harmonics with $\omega = \omega_{r3} = 3\omega_r$:

$$\begin{aligned} i_{0m}' &= i_{0m}^3 \sin(3\omega_1)t + i_{0m}^9 \sin(9\omega_1)t + \ldots \\ &\approx I_{0m}^3 \sin(3\omega_1)t \end{aligned} \tag{23}$$

The zero-sequence modulation compensation signal is required to compensate for the waveforms at a frequency three times that of the fundamental frequency. However, the PI controller generally faces limitations in responding to this high-frequency component due to its restricted bandwidth. Consequently, this paper applies the transfor- mation technique to solve this problem.

2) CONTROL SCHEME

The proposed control scheme is shown in Fig. 10(b). The harmonic suppression scheme is applied to the primary inverter only for avoiding the hunting problem. The 3rd-order harmonic zero-sequence circulating current $i_{0m3}^{'}$ is extracted by a speed-adapted band-pass filter $H_{BP}(s)$. A hypothesized quadrature current is generated by a phase shifter with 90-degree [16]. Then the two-phase currents are transformed into the 3rd-order harmonic rotating dq-domain. By treating the DC quantities by the proposed current control scheme and adding the cross coupling feedforward controls, the zero-sequence suppression compensated control voltage $v_{cont0,\alpha}$ is yielded and injected into the PWM schemes. The designed speed-adopted band-pass filter and current control scheme are summarized below.

a: BAND-PASS FILTER

$$H_{BP}(s) = \frac{\omega_m/Qs}{s^2 + \omega_m/Qs + \omega_m^2} \tag{24}$$

$$\omega_m = 2\pi f_c, f_c = 3n/(120/P) = 3n/20 \tag{25}$$

where, n = rotor speed in rpm, and pole number $P = 6$.

b: CURRENT CONTROL SCHEME

Due to the difficulty in accurate dynamic modeling, a roughly set PI feedback controller is augmented with a simple robust controller to yield the satisfactory dynamic response.

i) Current feedback controller:

The PI feedback controller is set as:

$$G_{ci}(s) = K_{Pi} + \frac{K_{Ii}}{s} = 3.5 + \frac{20}{s} \tag{26}$$

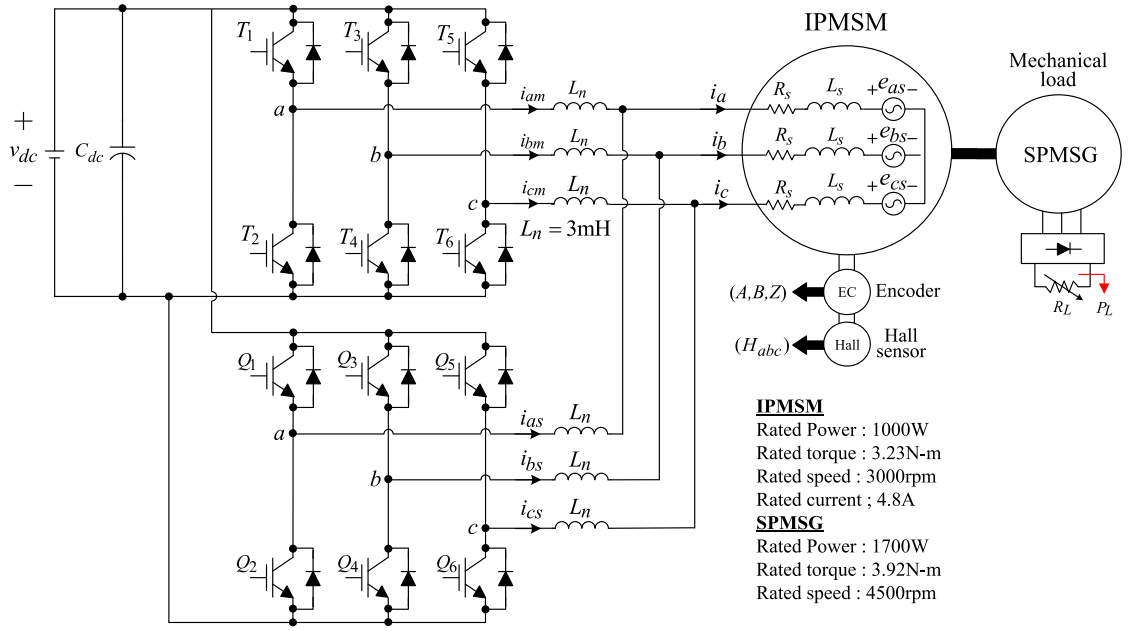

(a)

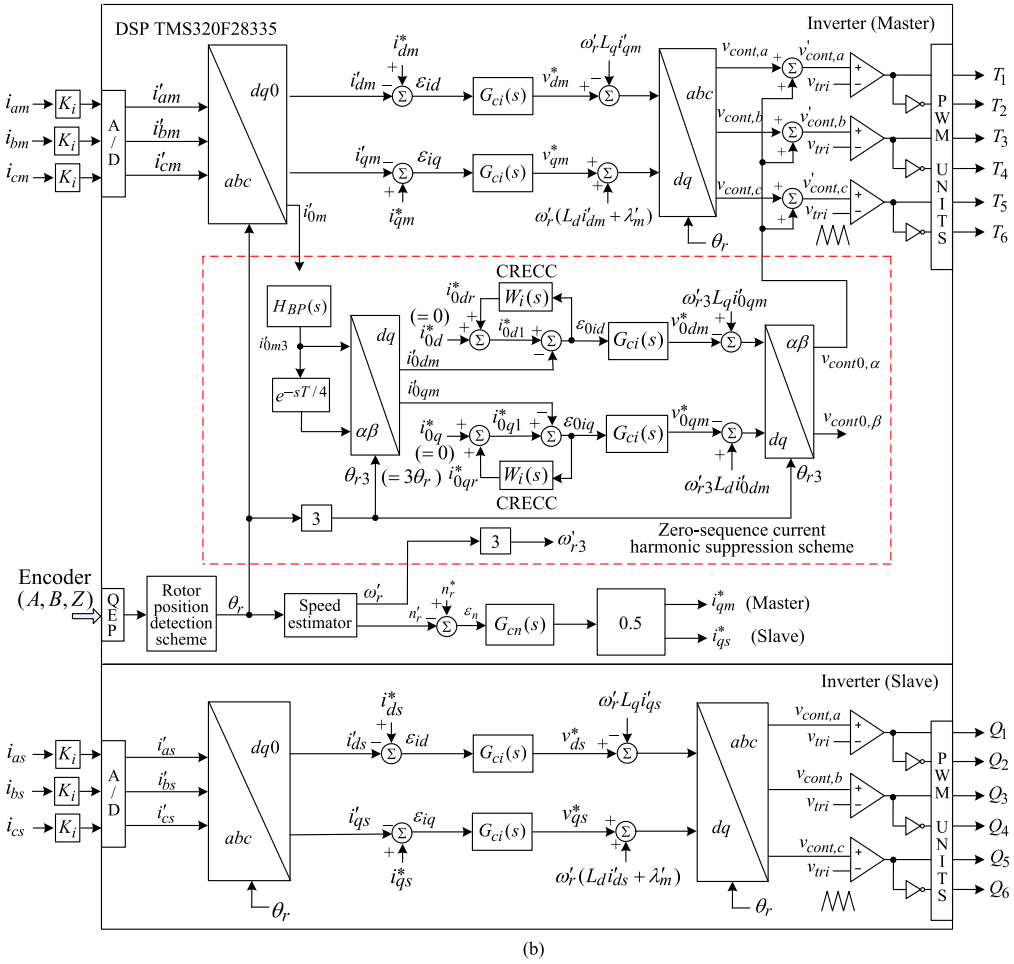

(b)

FIGURE 10. The developed dual-inverter fed PMSM drive: (a) power circuit; (b) control scheme.

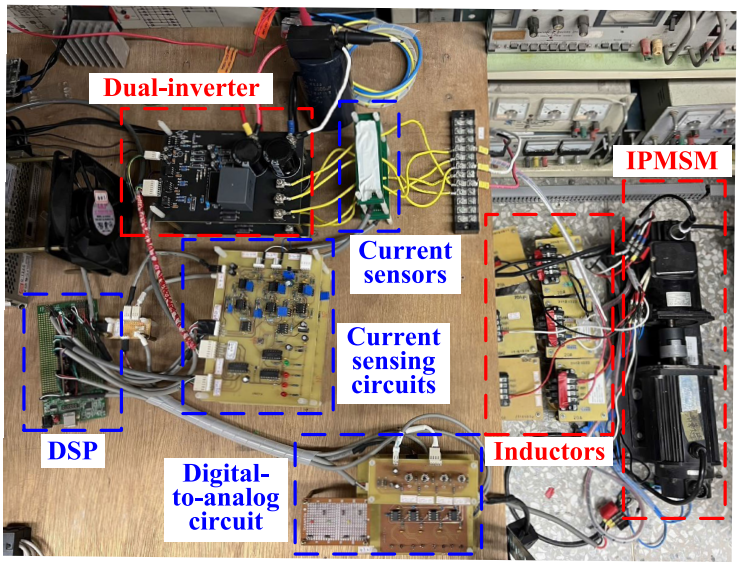

(c)

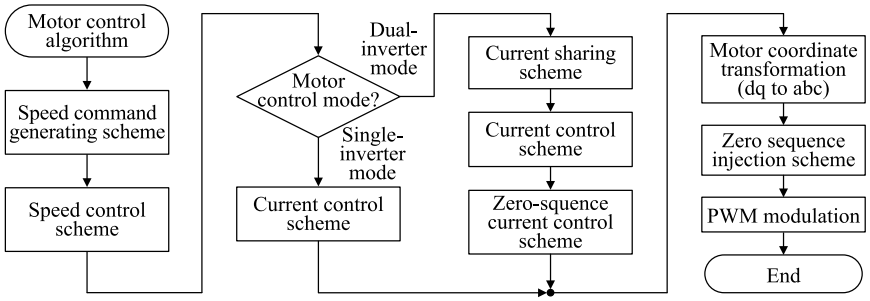

(d)

FIGURE 10. *(Continued.)* **The developed dual-inverter fed PMSM drive: (c) photo of experimental setup; (d) control flowchart.**

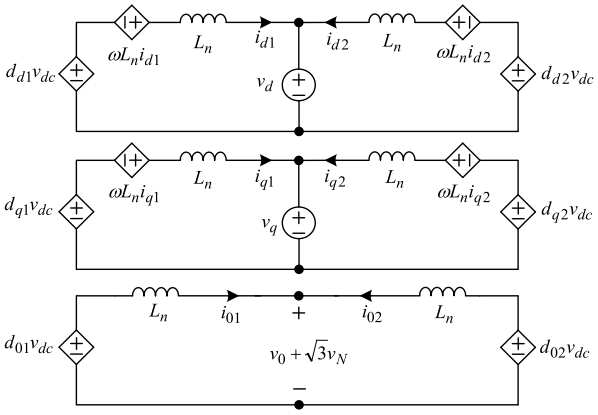

FIGURE 11. **Equivalent circuits of dual paralleled inverters.**

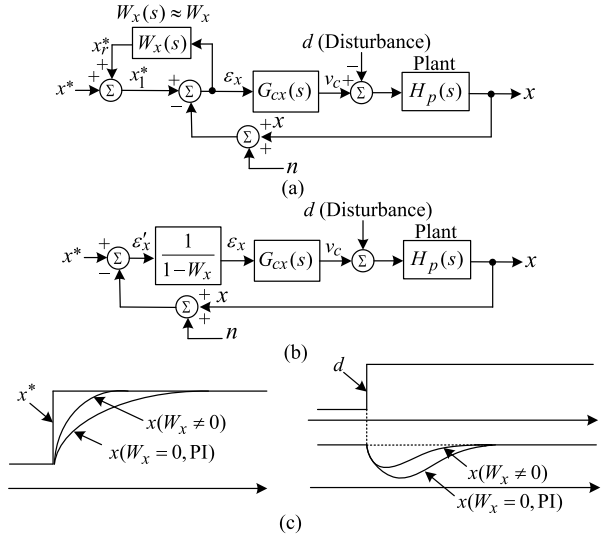

FIGURE 12. **The proposed unified CRECC: (a) original control block; (b) equivalent control block; (c) resulted step command tracking and disturbance regulation responses.**

ii) Current robust error cancellation controller (CRECC):

Taking the d-axis control scheme shown in Fig. 10(b) as an example, the original command i_{0d}^* is augmented by a robust control command $i_{0dr}^* = W_i(s)\varepsilon_{0id}$ to yield the modified command i_{0d1}^* to achieve the robust control. The effectiveness of the proposed CRECC is explained theoretically below.

Robustness analysis: Fig. 12(a) shows the proposed unified CRECC, where x^* is the command, x is the feedback variable, d denotes the disturbance, $H_p(s)$ is the plant dynamic model, n is the system contaminated noise, and v_c is the resulted

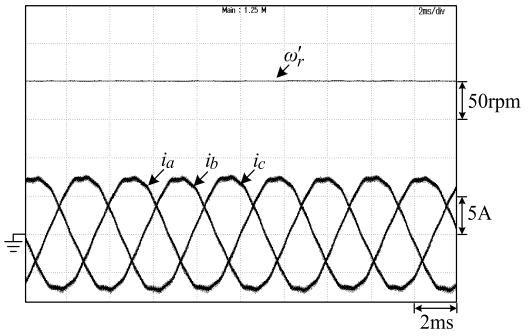

FIGURE 13. Measured (n_r',(i_a, i_b, i_c)) of the single-inverter fed PMSM drive at (n_r = 3000rpm, P_L = 1100W).

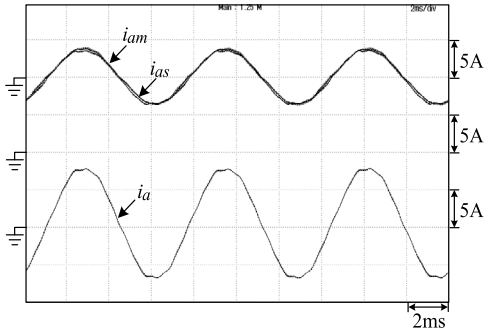

FIGURE 14. Measured ((i_{am}, i_{as}), i_a) of the dual-inverter fed PMSM drive at (n_r = 3000rpm, P_L = 1000W).

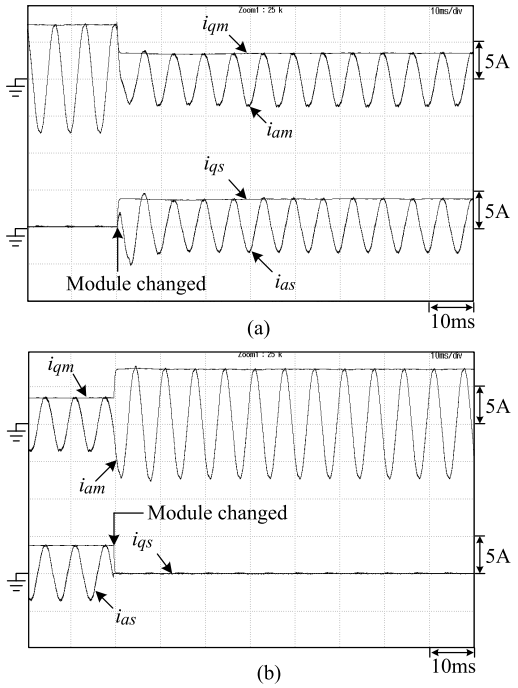

FIGURE 15. Measured (i_{qm}, i_{am}) and (i_{qs}, i_{as}) of the PMSM drive using IGBT IPM PSS20S92 at (n_r = 3000rpm, P_L = 1000W) due to the transitions: (a) from single-inverter to dual-inverter; (b) from dual-inverter to single-inverter.

control effort. The variable x represents the current here. The robust control weighting function is expressed as:

$$W_x(s) = \frac{W_x}{1 + \tau_x s} \approx W_x, 0 \le W_x < 1 \qquad (27)$$

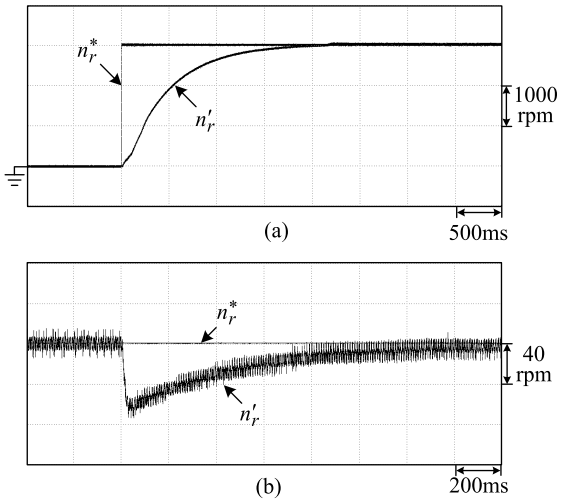

FIGURE 16. Measured speed responses of the single-inverter fed PMSM drive: (a) due to speed command change n_r^* → 3000rpm at P_L = 250W; (b) due to step load power change P_L = 500W → 1000W at n_r = 3000rpm.

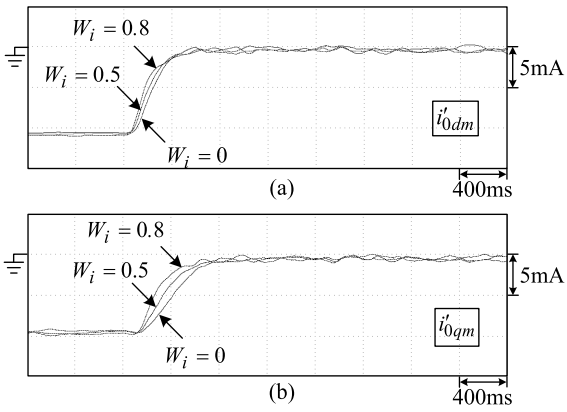

FIGURE 17. Measured i'_{0qm} and i'_{0dm} of the dual-inverter fed PMSM drive at (n_r = 3000rpm, P_L = 1000W) due to the suddenly added zero-sequence harmonic suppression.

where W_x is the robust control weighting factor, and the low-pass filtering process is employed to reduce the system noise effects. It can be reasonably assumed that $W_x(s) \approx W_x$ within the main dynamic frequency range.

Through careful derivation from Fig. 12(a), one can yield the equivalent control block depicted in Fig. 12(b) and the following attributes:

- The proportional and integral gains of PI controller are simultaneously magnified by $1/(1 - W_x)$. Equivalently, the tracking error is reduced from $\varepsilon_x \equiv x^* - x$ by PI control only to $\varepsilon_x' \equiv (1 - W_x)\varepsilon_x$ by adding the robust control. Fig. 12(c) sketches the resulted step command tracking and step disturbance regulation responses by adding the CRECC.
- The system noise n and the control effort v_c will be magnified by a factor of $1/(1 - W_x)$.

Hence the choice of W_x must be made taking the compromised considerations between the desired perfor- mance and the effects of magnified system noise and control effort.

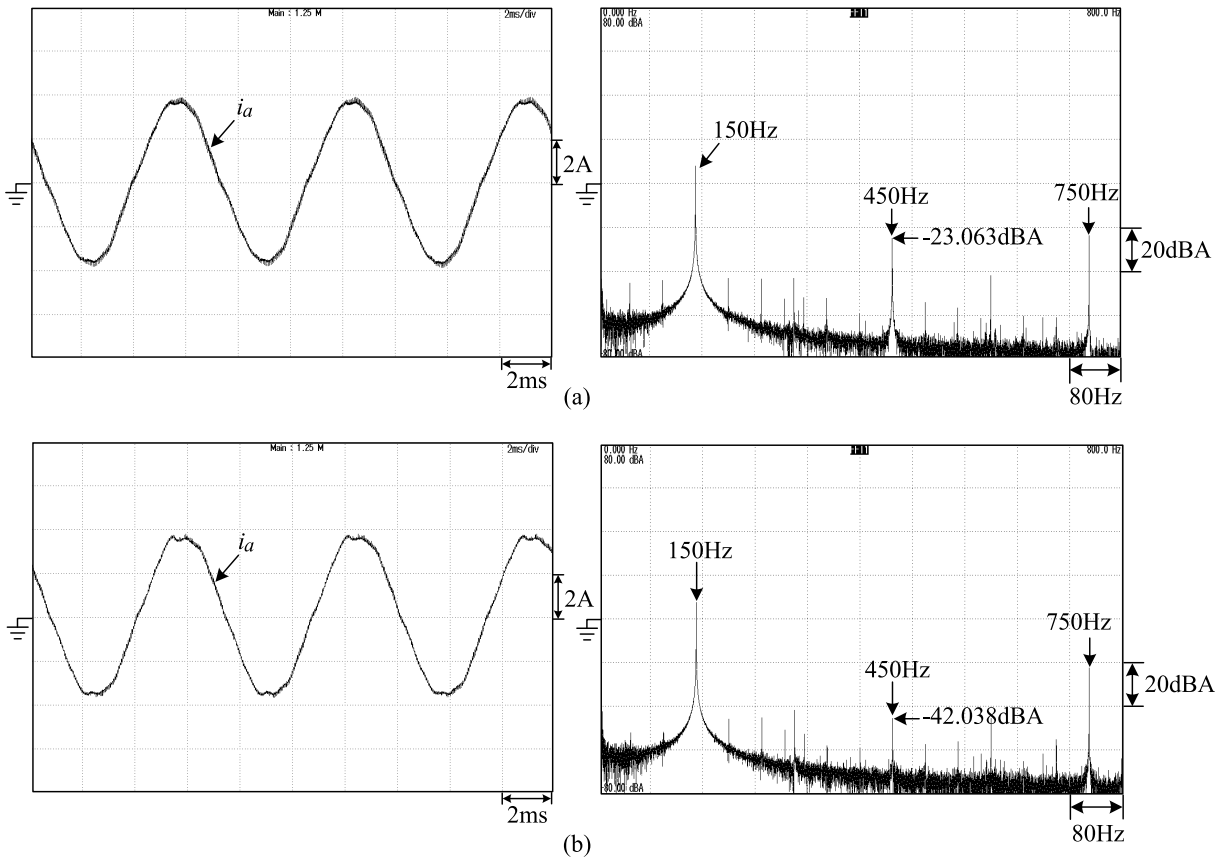

FIGURE 18. Measured i_{as} and its spectra of the dual-inverter fed PMSM drive at (n_r = 3000rpm,P_L = 1000W): **(a) without harmonic suppression; (b) with harmonic suppression.**

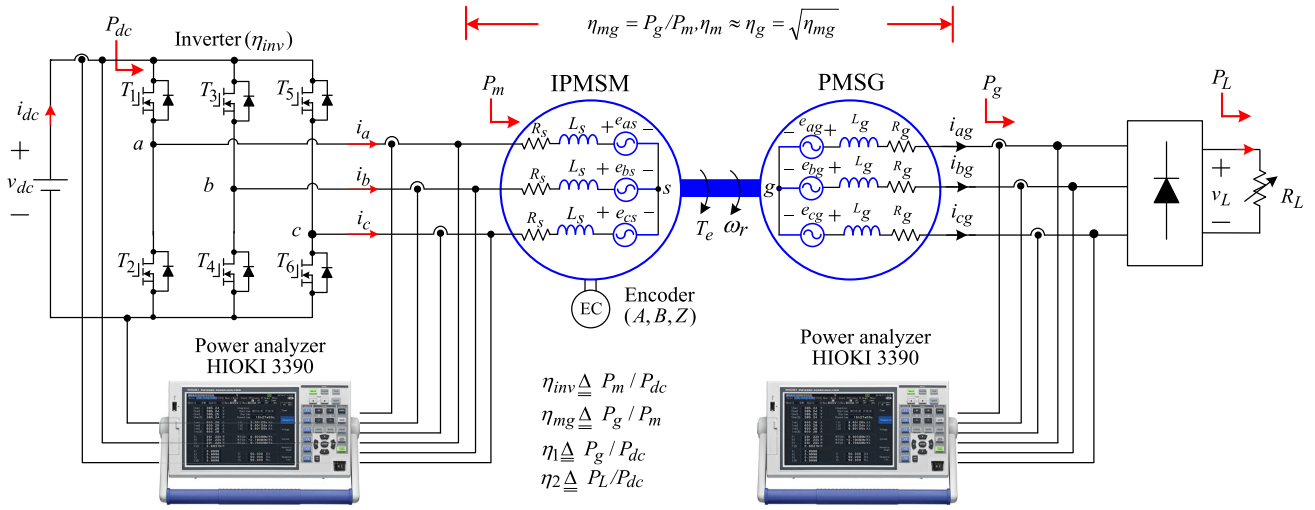

FIGURE 19. System configuration of efficiency measurement for the developed IPMSM drive.

IV. EXPERIMENTAL PERFORMANCE EVALUATION

A. BASIC CHARACTERISTICS

The developed single-inverter and dual-inverter fed PMSM drive depicted in Fig. 1 and Fig. 10 have been established. Some measured results are provided to verify the operating performances. The conditions set in making the tests are: (i)v_{dc} = 300V; (ii)f_s = 20kHz; and (iii) the IPM PSS20S92 is used.

Fig. 13 shows the measured (n_r', (i_a, i_b, i_c)) of the single-inverter fed PMSM drive at (n_r = 3000rpm,P_L = 1100W). And the ((i_{am}, i_{as}), i_a) of the dual-inverter fed PMSM drive are plotted in Fig. 14.

TABLE 2. Measured steady-state characteristics of single-inverter fed PMSM drive using the IPM PSS10S92 under different speeds and loads with switching frequency of 20 kHz.

Conditions	n_r =1000rpm, P_L = 55W			n_r =1500rpm, P_L =125W		
V_{dc} (V)	250	300	350	250	300	350
P_{dc} (W)	102.47	105.39	108.87	199.27	202.73	206.6
P_m (W)	93.2	94.1	95.1	187.1	188.3	189.8
P_σ (W)	56.8	56.8	56.8	127.7	127.7	127.7
P_L (W)	55	55	55	124.9	124.9	124.9
η_{inv} (%)*	90.95	89.3	87.31	93.89	92.9	91.85
$\eta_{m\sigma}$ (%)*	60.94	60.36	59.73	68.25	67.82	67.28
η_2 (%)*	53.67	52.19	50.52	62.68	61.61	60.45
Conditions	n_r = 2000rpm, P_L = 225W			n_r = 2500rpm, P_L = 350W		
V_{dc} (V)	250	300	350	250	300	350
P_{dc} (W)	331.7	335.45	340.14	492.47	497.2	501.94
P_m (W)	316.2	317.6	319.3	473.3	475.1	476.7
P_σ (W)	228.4	228.4	228.4	354.3	354.3	354.3
P_L (W)	224.5	224.6	224.5	349.7	349.7	349.7
η_{inv} (%)*	95.34	94.69	93.88	96.1	95.56	94.98
$\eta_{m\sigma}$ (%)*	72.23	71.91	71.53	74.86	74.57	74.32
η_2 (%)*	67.68	66.95	66	71.01	70.33	69.67
Conditions	n_r = 3000rpm, P_L = 500W					
V_{dc} (V)	250	300	350			
P_{dc} (W)	674	683.7	689.29			
P_m (W)	655.5	657.7	659.7			
P_σ (W)	505	505	505			
P_L (W)	499.4	499.5	499.5			
η_{inv} (%)*	97.25	96.19	95.71			
$\eta_{m\sigma}$ (%)*	77.04	76.78	76.55			
η_2 (%)*	74.09	73.06	72.47			

* $\eta_{inv} \equiv P_m/P_{dc}, \eta_{mg} \equiv P_g/P_m, \eta_2 \equiv P_L/P_{dc}$

The fault-tolerant and dynamic current sharing characteristics of the established dual-inverter fed PMSM drive are verified. Initially, the motor drive is stably operated at (n_r = 3000rpm, P_L = 1000W) with only the primary inverter module. Then the secondary inverter module is added and removed suddenly. The measured (i_{qm}, i_{am}) and (i_{qs}, i_{as}) of the primary and secondary inverters are respectively plotted in Fig. 15 (a) and 15(b). Normal operation with seamless transferred and good current sharing responses between the primary and secondary inverters can be observed from the results.

The speed tracking and load regulation responses are shown in Figs. 16(a) and 16(b), respectively. From these measured results. One can observe the normal operations and good performances in: (i) PMSM drives with single-inverter and dual-inverter; (ii) the transient responses under the changes between inverter schematics; and (iii) dynamic and steady-state characteristics.

In the proposed CRECC shown in Fig. 10(b), the robust control weighting function is set to be:

$$W_i(s) = \frac{W_i}{1 + \tau_i s}, 0 \le W_i < 1 \tag{28}$$

where $\tau_i = 1/(5 \times 150 \times 2\pi) = 2.12 \times 10^{-4}$s. The measured ($i'_{0dm}, i'_{0qm}$) of the dual-inverter fed PMSM drive due to the sudden addition of the developed harmonic supper- ssion approach without ($W_i = 0$) and with CRECC are plotted in Fig. 17. Successful operation can be seen. The faster elimination response by adding the CRECC can be observed. The effectiveness of the proposed CRECC analyzed theoretically above can be verified. The $W_i = 0.8$ is chosen here.

Under steady-state, the measured i_a and it spectra without and with harmonic suppression are compared in Figs. 18(a) and 18(b). From the labeled 3rd harmonics components, the magnitude is reduced from (-23.063dBA) without suppression to (-42.038dBA) with suppression. The significant reduction of zero-sequence current third-order harmonic magnitude can be observed.

B. EFFICIENCY ASSESSMENT

In conducting efficiency enhancement for an inverter fed motor drive, the normal running with properly designed power circuit and control schemes must be first possessed. The efficiency is affected by many factors, which are explored experimentally in this paper.

The system configuration of efficiency measurement for the established motor drive is shown in Fig. 19, wherein the definitions of efficiencies are labeled. The M-G set composite efficiency is defined as η_{mg} and the motor efficiency is assumed to be $\eta_m \approx \eta_g = \sqrt{\eta_{mg}}$. Two HIOKI 3390 power meters are employed to measure the efficiencies of the inverter, the IPMSM and the SPMSG. The single-inverter

TABLE 3. Measured steady-state characteristics of single-inverter fed PMSM drive using the IPM PSS20S92 under different speeds and loads with switching frequency of 20 kHz.

Conditions	n_r =1000rpm, P_L =100W			n_r =1500rpm, P_L =250W		
V_{dc} (V)	250	300	350	250	300	350
P_{dc} (W)	166.4	170.5	175	361.6	366.4	371.5
P_m (W)	144.6	145.1	145.6	332.9	333.8	334.8
P_g (W)	103	103	104	256	256	256
P_L (W)	101.4	101.4	101.5	252.3	252.3	252.3
η_{inv} (%)*	86.89	85.1	83.22	92.05	91.11	90.13
η_{mg} (%)*	71.23	70.99	71.43	76.9	76.69	76.46
η_2 (%)*	60.94	59.47	58	69.77	68.86	67.91
Conditions	n_r = 2000rpm, P_L = 450W			n_r = 2500rpm, P_L = 700W		
V_{dc} (V)	250	300	350	250	300	350
P_{dc} (W)	612.7	618.2	624.7	929.5	935.5	942.4
P_m (W)	576.4	577.5	579.2	883.6	884.5	886.3
P_g (W)	458	458	459	708	708	707
P_L (W)	452	452	453	700.9	700.9	700.8
η_{inv} (%)*	94.08	93.41	92.72	95.06	94.55	94.05
η_{mg} (%)*	79.46	79.31	79.25	80.13	80.05	79.77
η_2 (%)*	73.77	73.12	72.51	75.41	74.92	74.36
Conditions	n_r = 3000rpm, P_L =1kW					
V_{dc} (V)	250	300	350			
P_{dc} (W)		1342.9	1353.7			
P_m (W)		1282.1	1283.7			
P_g (W)		1041	1041			
P_L (W)		1031.9	1032.1			
η_{inv} (%)*		95.47	94.83			
η_{mg} (%)*		81.19	81.09			
η_2 (%)*		76.84	76.24			

* $\eta_{inv} \equiv P_m/P_{dc}, \eta_{mg} \equiv P_g/P_m, \eta_2 \equiv P_L/P_{dc}$

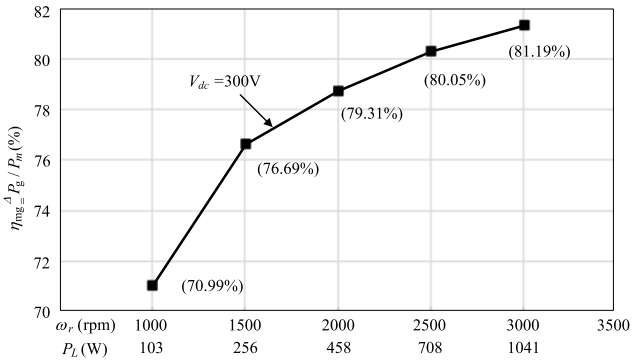

FIGURE 20. Measured M-G set efficiencies η_{mg} under different speeds and loads.

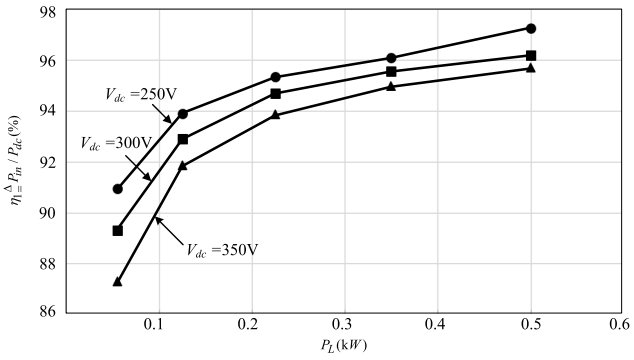

FIGURE 21. Measured efficiency curves of the single-inverter using the IPM PSS10S92 under different DC-link voltages and loads.

and dual-inverter are respectively constructed using one IPM PSS20S92, one IPM PSS10S92, and two IPMs PSS10S92. The mechanical load is adjusted by the load resistance R_L. The load power is increased with the increased speed. The switching frequencies in all cases are all set at f_s = 20kHz.

The motor efficiency is less effected by the DC-link voltage level. Fig. 20 plots the efficiency curve η_{mg} vs. load (speed) with v_{dc} = 300V. The results indicate that the machine efficiency is increased with load level. Under P_L = 1041W(n_r = 3000rpm), $\eta_m \approx \sqrt{0.8119} = 90.11\%$ is found.

Fig. 21 plots the measured efficiency curves of the single-inverter using the smaller IPM PSS10S92 under various DC-link voltages and loads up to P_L = 500W for lower rating. Fig. 22 shows the efficiency curves of the single-inverter formed by the larger IPM PSS20S92 under v_{dc} = 300V and 350V up to 1kW. But the load power can only reach about P_L = 700W under v_{dc} = 250V due to the effects of back-EMF. And results of the dual-inverter using the IPM PSS10S92 under the same conditions of Fig. 22 are plotted in Fig. 23. The detailed data corresponding to Figs. 21 to 23 are listed in Tables 2 to 4.

TABLE 4. Measured steady-state characteristics of dual-inverter fed PMSM drive using the IPM PSS10S92 under different speeds and loads with switching frequency of 20 kHz.

Conditions	$n_r = 1000$rpm, $P_L = 110$W			$n_r = 1500$rpm, $P_L = 250$W		
V_{dc} (V)	250	300	350	250	300	350
P_{dc} (W)	183.9	191.9	201	366.4	375.2	385.4
P_m (W)	155.8	155.7	155.5	332.7	332.8	332.9
P_g (W)	113.5	113.4	113.5	256.1	256.1	256.1
P_L (W)	109.6	109.5	109.6	250	249.9	250
η_{inv} (%)*	84.74	81.11	77.35	90.79	88.69	86.39
η_{mg} (%)*	72.85	72.83	72.99	76.98	76.95	76.93
η_2 (%)*	59.6	57.06	54.53	68.23	66.6	64.87
Conditions	$n_r = 2000$rpm, $P_L = 450$W			$n_r = 2500$rpm, $P_L = 700$W		
V_{dc} (V)	250	300	350	250	300	350
P_{dc} (W)	617.3	627.6	638.8	926.4	938.1	950.5
P_m (W)	577.7	578.2	578.8	881.4	881.7	882.5
P_g (W)	457.7	457.6	457.7	711	711	711
P_L (W)	449.2	449.1	449.1	700	700	700
η_{inv} (%)*	93.58	92.13	90.6	95.14	93.99	92.85
η_{mg} (%)*	79.23	79.14	79.08	80.67	80.64	80.57
η_2 (%)*	72.77	71.56	70.3	75.56	74.62	73.65
Conditions	$n_r = 3000$rpm, $P_L = 1$kW					
V_{dc} (V)	250	300	350			
P_{dc} (W)		1305.7	1320.8			
P_m (W)		1243.2	1243.9			
P_g (W)		1013.3	1013.2			
P_L (W)		1000.3	1000.2			
η_{inv} (%)*		95.21	94.18			
η_{mg} (%)*		81.51	81.45			
η_2 (%)*		76.61	75.73			

* $\eta_{inv} \equiv P_m/P_{dc}, \eta_{mg} \equiv P_g/P_m, \eta_2 \equiv P_L/P_{dc}$

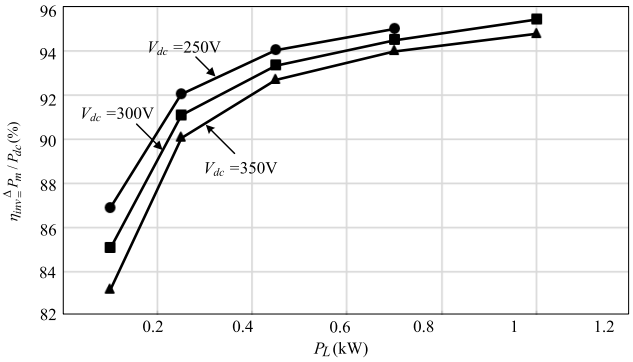

FIGURE 22. Measured efficiency curves of the single-inverter using the IPM PSS20S92 under different DC-link voltages and loads.

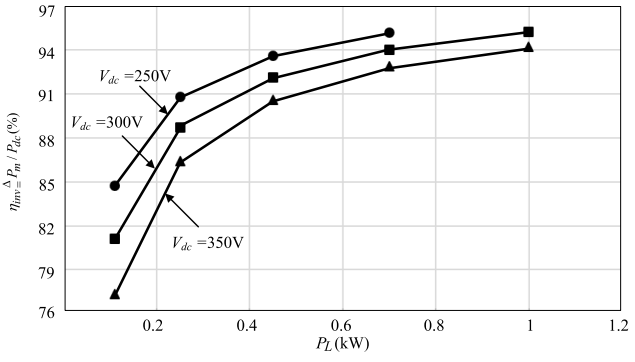

FIGURE 23. Measured efficiency curves of the dual-inverter using the IPM PSS10S92 under different DC-link voltages and loads.

From the above results one can find that: (i) Single-inverter using IPM PSS10S92 with lower rating can only be operated up to about 500W; (ii) As the voltage is enough, the efficiencies of the IPM-based inverter are increased for the lower DC-link voltage; (iii) Under lower DC-link voltage ($v_{dc} = 250$V), the PMSM drive will be failed to operate above a certain load power. This is mainly due to the increased speed-dependent back-EMF effects ($k_e = 28.74\text{V}_{\text{rms}}$/krpm for the employed motor). The comparative efficiencies of single-inverter and dual-inverter under various loads at $v_{dc} = 300$V are plotted in Fig. 24. Some facts can be deduced from the observation: (i) Within the same achievable power range ($\leq$ 500W), the IPM PSS10S92 (10ADC) possesses much larger efficiencies than the IPM PSS20S92 (20ADC); (ii) Single-inverter has higher efficiency than the dual-inverter. However, the difference is gradually reduced with the increased power level, and maybe even lower under heavier loads; and (iii) By adopting the dual-inverter with

TABLE 5. Measured steady-state characteristics of single-inverter fed PMSM drive using the IPM PSS10S92 under different speeds and loads with switching frequency of 5 kHz.

Conditions	n_r =1000rpm, P_L =20W			n_r =1500rpm, P_L =62.5W		
V_{dc} (V)	250	300	350	250	300	350
P_{dc} (W)	59.6	60.8	64.05	124.8	127.1	129.1
P_m (W)	56	58	61.6	119	121	122
P_g (W)	20.8	20.6	20.6	63.8	63.8	63.8
P_L (W)	20	20	20	62.4	62.5	62.5
η_{inv} (%)*	93.53	92.7	91.82	95.66	95.19	94.55
η_{mg} (%)*	37.14	35.52	33.44	53.61	52.73	52.3
η_2 (%)*	33.56	32.89	31.23	50	49.17	48.41
Conditions	n_r = 2000rpm, P_L =150W			n_r = 2500rpm, P_L = 300W		
V_{dc} (V)	250	300	350	250	300	350
P_{dc} (W)	242.7	244.8	246.7	429.7	432.7	436.2
P_m (W)	235	236	237	419	420	422
P_g (W)	152.5	152.4	152.4	303.9	303.9	303.9
P_L (W)	149.9	149.9	149.9	299.6	229.6	229.6
η_{inv} (%)*	96.73	96.45	96.01	97.41	97.13	96.82
η_{mg} (%)*	64.89	64.58	64.3	72.53	72.36	72.01
η_2 (%)*	61.76	61.23	60.76	69.72	53.06	52.64
Conditions	n_r = 3000rpm, P_L = 500W					
V_{dc} (V)	250	300	350			
P_{dc} (W)	673.1	679	683.8			
P_m (W)	658	662	665			
P_g (W)	505.7	505.8	505.8			
P_L (W)	499.3	499.3	499.3			
η_{inv} (%)*	97.79	97.50	97.29			
η_{mg} (%)*	76.85	76.4	76.06			
η_2 (%)*	74.18	73.53	73.02			

* $\eta_{inv} \equiv P_m/P_{dc}, \eta_{mg} \equiv P_g/P_m, \eta_2 \equiv P_L/P_{dc}$

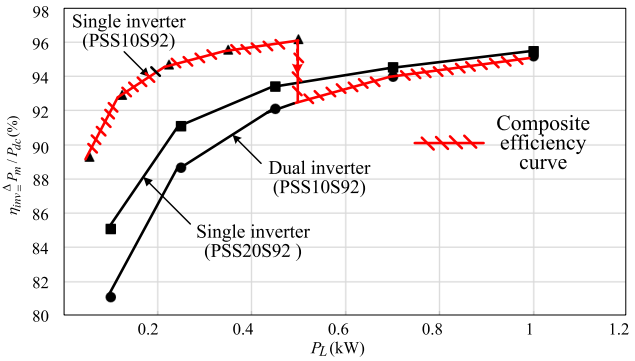

FIGURE 24. Measured efficiency curves of single-inverter and dual-inverter under different loads at v_{dc} = 300V.

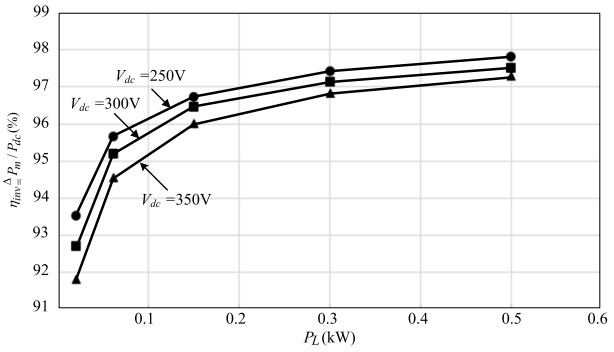

FIGURE 25. Measured efficiency curves of the single-inverter using the IPM PSS10S92 under different DC-link voltages and loads with switching frequency of 5kHz.

suitably rated IPM cell, the high composite efficiencies over all load range can be achieved as indicated in Fig. 24. Single-inverter is adopted below 500W, and dual-inverter is applied as the load power is above 500W.

C. EFFECTS OF SWITCHING FREQUENCY

Generally, the switching loss of an inverter will be dominant under light load and/or low speed. To explore this fact experimentally, the mechanical load power P_L is set to be $P_L \propto n_r^3$ for emulating the inherent pump load characteristics. Table 5 and Table 6 list the measured steady-state data of the single-inverter fed PMSM drives using the IPM PSS10S92 under the loads within P_L = 500W with the switching frequencies of 5kHz and 20kHz, respectively. The corresponding inverter efficiency curves are plotted in Figs. 25 and 26. Much higher efficiencies using lower switching frequency and lower DC-link voltages can be aware from the results. See for example:

TABLE 6. Measured steady-state characteristics of single-inverter fed PMSM drive using the IPM PSS10S92 under different speeds and loads with switching frequency of 20 kHz.

Conditions	n_r =1000rpm, P_L = 20W			n_r =1500rpm, P_L = 62.5W		
V_{dc} (V)	250	300	350	250	300	350
P_{dc} (W)	60	62.6	65.5	126.7	129.6	133
P_m (W)	53	54	54	118	118	119
P_g (W)	20.6	20.6	20.6	63.8	63.8	63.8
P_L (W)	20	20	20	62.5	62.5	62.6
η_{inv} (%)*	88.11	85.72	82.93	92.8	91.39	89.8
η_{mg} (%)*	38.87	38.15	38.15	54.07	54.07	53.61
η_2 (%)*	33.33	31.95	30.53	49.33	48.23	47.07
Conditions	n_r = 2000rpm, P_L = 150W			n_r = 2500rpm, P_L = 300W		
V_{dc} (V)	250	300	350	250	300	350
P_{dc} (W)	242.7	246.4	250.8	431.5	435.9	440.9
P_m (W)	230	232	233	414	416	418
P_g (W)	152.4	152.4	152.4	303.6	303.6	303.5
P_L (W)	150	150	150	299.5	299.5	229.5
η_{inv} (%)*	94.93	94.10	92.91	95.95	95.35	94.72
η_{mg} (%)*	66.26	65.69	65.41	73.33	72.98	72.61
η_2 (%)*	61.8	60.88	59.81	69.41	68.71	52.05
Conditions	n_r = 3000rpm, P_L = 500W					
V_{dc} (V)	250	300	350			
P_{dc} (W)	673.1	683	687.6			
P_m (W)	654	656	657			
P_g (W)	505.3	505.3	505.3			
P_L (W)	499.3	499.2	499.2			
η_{inv} (%)*	96.55	95.98	95.55			
η_{mg} (%)*	77.26	77.03	76.91			
η_2 (%)*	74.18	73.09	72.6			

* $\eta_{inv} \equiv P_m/P_{dc}, \eta_{mg} \equiv P_g/P_m, \eta_2 \equiv P_L/P_{dc}$

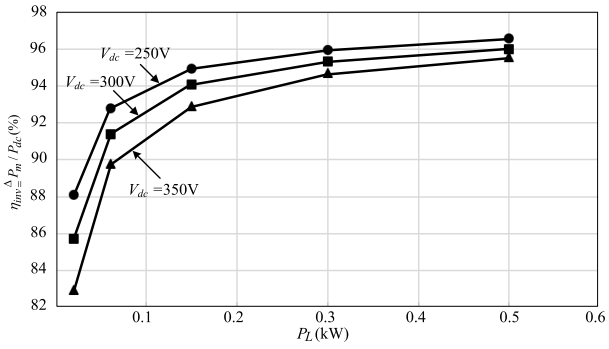

FIGURE 26. Measured efficiency curves of the single-inverter using the IPM PSS10S92 under different DC-link voltages and loads with switching frequency of 20kHz.

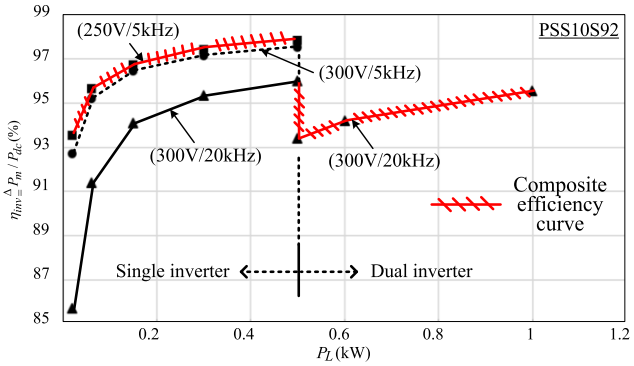

FIGURE 27. Measured composite efficiency curves of single-inverter and dual-inverter over wide speed range considering DC-link voltage and switching frequency.

- V_{dc} = 250V, P_L = 20W:
  η_{inv} = 93.53%(f_s =5kHz);
  η_{inv} = 88.11%(f_s =20kHz).
- V_{dc} = 250V, P_L = 500W:
- η_{inv} = 97.79%(f_s =5kHz);
- η_{inv} = 96.55%(f_s =20kHz).

Based on the explored results, the composite efficiency curves modified from Fig. 24 are plotted in Fig. 27, wherein below 500W, the inverter operation with lower switching frequency and lower DC-link voltage (v_{dc} = 250V/f_s = 5kHz) is suggested. Above 500W, the setting (300V/20kHz) is applied instead. The improved efficiencies over wide speed range dedicated for pump load can be achieved.

Comments: (1) For a specific motor, its key variables must be adequately tuned for enhancing the developed torque and thus the energy conversion efficiency. See for example, the commutation shifting for IPMSM and synchronous

reluctance motor, and the slip angular speed command setting for vector controlled induction motor. Above rated speed, the proper field-weakening via field current command setting (i_d^* in Fig. 1(b)) or equivalently via advanced commutation shifting (β-angle in Fig. 1(b)) to counteract the effects of back-EMF. As the speed is further increased, the effect of commutation shift is limited. The DC-link voltage boosting must be applied for avoiding the rotor magnet demagnetization due to excess field-weakening; (2) An inverter fed AC motor drive powered from the mains may preserve the evenly high efficiencies over wide operation range by equipping a suited switch-mode rectifier to vary the DC-link voltage. Meanwhile, good line drawn AC power quality can be obtained; (3) As the motor speed is increased, the fundamental frequency and load level are increased. For enhancing the stable operation with lower switching ripples, the switching frequency must be increased.

V. CONCLUSION

Normally, a motor drive may be often operated in partial and light loads, such as motor driven fan and pump loads. This paper has presented the IPM-based dual-inverter fed PMSM drive having evenly high efficiency over wide speed/load ranges under satisfactory driving performance. Various key affecting factors are explored experimentally. The single-inverter fed motor drive is first established. Through the properly designed power circuit, current and speed control schemes, good driving performances are preserved. The dynamic modeling and systematic controller designs for current and speed loops are made. Then, the dual-inverter powered PMSM is developed. The good current sharing control is obtained by the designed current control scheme. In circulating zero-sequence current suppression control, a mathematical model is derived. And an effective zero-sequence harmonic suppression scheme is proposed. The major 3rd-order circulating zero-sequence current harmonic is extracted by a speed-adapted band-pass filter. Then a hypothesized quadrature current component is generated. The 3rd-order two-phase currents are transformed into the 3rd-order harmonic rotating dq-frame. Through regulating the DC quantities, the bandwidth limitation of the PI-controller is avoided. In addition, a simple CRECC is proposed to increase the suppression control response speed and robustness. The effectiveness in harmonic reduction has been demonstrated theoretically and experimentally.

Having satisfactory driving characteristics under various operating conditions, the key effects on efficiency were explored experimentally, including IPM type, number of working inverters, DC-link voltage level, and switching frequency, etc. Some facts deduced include: (i) The motor efficiency depends on load level and is less affected by DC-link voltage level. Hence, the employment of over rated motor must be avoided. For a specific motor, the proper tuning its key variables can further enhance the efficiency; (ii) Too low DC-link voltage will let the motor drive be failed to operate above a certain speed due to the effects of motor back-EMF. Above the rated speed, the proper field-weakening must be applied under fixed rated DC-link voltage. As the speed is further increased, the DC-link voltage boosting approach can be a better alternative approach; (iii) If the DC-link voltage is sufficient, the lower DC-link voltage possesses higher inverter efficiency; (iv) Under lower speed and lighter loads, the IPM with smaller current rating has higher efficiency. The lower DC-link voltage and switching frequency can be adopted to further increase the efficiency; (v) The high composite efficiency over wide speed/load ranges can be preserved as depicted in Fig. 27 by adopting dual inverters with lower ratings and applying proper working number determination according to load level.

REFERENCES

[1] Z. Ye, P. K. Jain, and P. C. Sen, "Circulating current minimization in high-frequency AC power distribution architecture with multiple inverter modules operated in parallel," *IEEE Trans. Ind. Electron.*, vol. 54, no. 5, pp. 2673–2687, Oct. 2007.

[2] S. Fukuda, "A control method for parallel-connected multiple inverter systems," in *Proc. 7th Int. Conf. Power Electron. Variable Speed Drives*, 1998, pp. 175–180.

[3] Z. Ye, D. Boroyevich, J.-Y. Choi, and F. C. Lee, "Control of circulating current in two parallel three-phase boost rectifiers," *IEEE Trans. Power Electron.*, vol. 17, no. 5, pp. 609–615, Sep. 2002.

[4] J. S. Siva Prasad and G. Narayanan, "Minimization of grid current distortion in parallel-connected converters through carrier interleaving," *IEEE Trans. Ind. Electron.*, vol. 61, no. 1, pp. 76–91, Jan. 2014.

[5] D. Sha, Z. Guo, and X. Liao, "Control strategy for input-parallel–output-parallel connected high-frequency isolated inverter modules," *IEEE Trans. Power Electron.*, vol. 26, no. 8, pp. 2237–2248, Aug. 2011.

[6] Y. Chen and K. M. Smedley, "One-cycle-controlled three-phase grid connected inverters and their parallel operation," *IEEE Trans. Ind. Appl.*, vol. 44, no. 2, pp. 663–671, Apr. 2008.

[7] J. Thunes, R. Kerkman, D. Schlegel, and T. Rowan, "Current regulator instabilities on parallel voltage-source inverters," *IEEE Trans. Ind. Appl.*, vol. 35, no. 1, pp. 70–77, Jan. 1999.

[8] H. Cai, R. Zhao, and H. Yang, "Study on ideal operation status of parallel inverters," *IEEE Trans. Power Electron.*, vol. 23, no. 6, pp. 2964–2969, Nov. 2008.

[9] W. Hu, Y. Wang, W. Yao, H. Zhang, J. Wu, and Z. Wang, "Modeling and control of zero-sequence current in multiple grid connected converter," in *Proc. IEEE Power Electron. Specialists Conf.*, Rhodes, Greece, Jun. 2008, pp. 2064–2069.

[10] D. Panprasert and B. Neammanee, "The D and Q axes technique for suppression zero-sequence circulating current in directly parallel three-phase PWM converters," *IEEE Access*, vol. 9, pp. 52213–52224, 2021, doi: 10.1109/ACCESS.2021.3069702.

[11] K. M. Rahman and S. Hiti, "Identification of machine parameters of a synchronous motor," *IEEE Trans. Ind. Appl.*, vol. 41, no. 2, pp. 557–565, Mar. 2005.

[12] M. P. Kazmierkowski and L. Malesani, "Current control techniques for three-phase voltage-source PWM converters: A survey," *IEEE Trans. Ind. Electron.*, vol. 45, no. 5, pp. 691–703, Oct. 1998.

[13] T. Li, X. Sun, M. Yao, D. Guo, and Y. Sun, "Improved finite control set model predictive current control for permanent magnet synchronous motor with sliding mode observer," *IEEE Trans. Transport. Electrific.*, vol. 10, no. 1, pp. 699–710, Mar. 2023.

[14] T. Li, X. Sun, G. Lei, Y. Guo, Z. Yang, and J. Zhu, "Finite-Control-Set model predictive control of permanent magnet synchronous motor drive systems—An overview," *IEEE/CAA J. Autom. Sinica*, vol. 9, no. 12, pp. 2087–2105, Dec. 2022.

[15] Y. Tang, W. Xu, Y. Liu, and D. Dong, "Dynamic performance enhancement method based on improved model reference adaptive system for SPMSM sensorless drives," *IEEE Access*, vol. 9, pp. 135012–135023, 2021.

[16] J. Benjanarasut and B. Neammanee, "The D-, Q- axis control technique of single phase grid connected converter for wind turbines with MPPT and anti-islanding protection," in *Proc. 8th Electr. Eng. Electron., Comput., Telecommun. Inf. Technol. (ECTI) Assoc. Thailand Conf.*, May 2011, pp. 649–652, doi: 10.1109/ECTICON.2011.5947923.

YI-SHI LIN was born in Tainan, Taiwan, in February 2000. He received the B.S. degree in electronic engineering from the National Taiwan University of Science and Technology, Taipei, Taiwan, in 2022. He is currently pursuing the M.S. degree in electrical engineering with National Tsing Hua University, Hsinchu, Taiwan. His research interests include power electronics, motor drives, microgrids, and digital converter.

CHEN-WEI YANG was born in Yunlin, Taiwan, in August 1995. He received the B.S. degree in electrical engineering from the National Taipei University of Technology, Taipei, Taiwan, in 2017. He is currently pursuing the Ph.D. degree in motor drive with National Tsing Hua University, Hsinchu, Taiwan. His research interests include power electronics, motor drives, and electric machine control.

CHANG-MING LIAW (Member, IEEE) was born in Taichung, Taiwan, in June 1951. He received the B.S. degree in electronic engineering from the Evening Department, Tamkang College of Arts and Sciences, Taipei, Taiwan, in 1979, and the M.S. and Ph.D. degrees in electrical engineering from National Tsing Hua University, Hsinchu, Taiwan, in 1981 and 1988, respectively.

In 1988, he joined as a Faculty Member of the Department of Electrical Engineering, National Tsing Hua University, as an Associate Professor. Since 1993, he has been a Professor with the Department of Electrical Engineering. His research interests include power electronics, motor drives, and electric machine control. He is a Life Member of Chinese Institute of Electrical Engineering (CIEE), an Editorial Board Member of *Advances in Power Electronics* (Hindawi), and an Editor of *International Journal of Electrical Engineering* (ROC).

CHANG-LIN CHIANG received the B.S. and M.S. degrees in electronic engineering from Chung Yuan Christian University, Taiwan, and the Ph.D. degree in electrophysics from National Chiao Tung University, Taiwan, in 2016. In 2016, he joined the Green Environment and Environment Research Laboratories (GEL), ITRI, Hsinchu, Taiwan. His research interests include motor drive, eddy current sensor, gas bearing, flight simulator mechanism and system integration technologies, gas discharge mechanism and physical behavior, and evaporation technologies. He was a recipient of the Patent Map Competition Award, in 2017.

YANG-GUANG LIU received the Ph.D. degree in mechanical engineering from National Chiao Tung University, Taiwan, in 2010. In 2010, he joined the Green Environment Laboratories (GEL), ITRI, Hsinchu, Taiwan. He is currently the Deputy Division Director of the High Efficiency Development Division, GEL-ITRI. He has also published over 28 articles, 22 patents, and 20 research reports during the past five-year. His research interests include compressor and PM-motor design with CAE analysis, programming tool for compressor design, and analysis and optimization. He was selected as the Outstanding Young Engineer from CIE Taiwan, in 2019.

CHIEN-CHANG WANG received the B.S. degree in physics from Soochow University, in 1997, the M.S. degree in physics from National Chung Cheng University, Taiwan, in 1999, and the Ph.D. degree in material and science and engineering from National Chiao Tung University, Taiwan, in 2008.

From 1999 to 2003, he was an Associate Engineer with the Optical Electronical System Laboratory, ITRI. From 2003 to 2012, he was an Engineer with the Green Energy and Environment Research Laboratories (GEL), ITRI. Since 2012, he has been an Senior Engineer with GEL, ITRI. His research interests include magnetic circuit design, micro motors, high-power and high-speed electric machines and applications, compressors, vibration and noise diagnostics, and heating and refrigeration applications. He was a recipient of the Research and Development 100 Awards, in 2015, and Chinese Institute of Electrical Engineering Outstanding Electrical Engineer Award, in 2019.